EPTT-2024-0040
A numerical simulation with OpenFOAM of a NACA0012 airfoil at high Reynolds number and critical angle of attack

Marcelo I. Adotti

Institute for Modeling and Technological Innovation, IMIT (CONICET-UNNE) and Aerodynamics Laboratory - Engineering Faculty, Universidad Nacional del Nordeste (UNNE), Avda. Las Heras 727 H3500 Resistencia, Argentina
italoadotti@conicet.gov.ar

Adrián R. Wittwer

Institute for Modeling and Technological Innovation, IMIT (CONICET-UNNE) and Aerodynamics Laboratory - Engineering Faculty, Universidad Nacional del Nordeste (UNNE), Avda. Las Heras 727 H3500 Resistencia, Argentina
a_wittwer@yahoo.es

William R. Wolf

School of Mechanical Engineering, Universidade Estadual de Campinas, Campinas, SP, 13083-860, Brazil

Horacio Aguerre

Centro de Investigación de Métodos Computacionales, CONICET-UNL, Santa Fe, Argentina

Gisela M. Alvarez y Alvarez

Aerodynamics Laboratory - Engineering Faculty, Universidad Nacional del Nordeste (UNNE), Avda. Las Heras 727 H3500 Resistencia, Argentina

Mario E. De Bortoli

Aerodynamics Laboratory - Engineering Faculty, Universidad Nacional del Nordeste (UNNE), Avda. Las Heras 727 H3500 Resistencia, Argentina

Abstract. *This study presents a numerical simulation of the flow around a NACA0012 airfoil with a high Reynolds number of $1x10^6$ and a critical angle of attack of 18º using OpenFOAM. The hybrid turbulence model $\kappa\omega_{SST}DDES$ is used to capture complex turbulent phenomena in the wake, produced by the detachment at the leading edge and reinsertion of the boundary layer on the airfoil and the detachment of the flow in the trailing edge. The simulations aim to improve the understanding of turbulent flow under stall conditions. The results are compared with reference literature.*

Keywords: *CFD, Turbulence, Hybrid RANS-LES, NACA0012*

1. INTRODUCTION

In Computational Fluid Dynamics (CFD), simulating turbulent flow around airfoils in a high angle-of-attack and stall-state configuration is a challenging task. Complex boundary layer effects at high Reynolds number conditions characterise these turbulent flows. Laminar to turbulent transition phenomena at the leading edge, flow detachment and reattachment in conjunction with detachment at the trailing edge are characteristic of turbulent flow around these airfoils. The study of these flows is crucial to understand the aerodynamic performance. The relationship between computational cost and high quality simulation of turbulent flow is defined by the turbulence model adopted.

Currently, methods such as Direct Numerical Simulation (DNS), Large Eddy Simulation (LES) and hybrid models of the Averaged Navier-Stokes Equations (RANS/LES) are widely used to simulate the type of flow described above. These can be used, depending on the computational capacity available and the Reynolds number of the phenomenon to be simulated. According to Ke and Edwards (2017), hybrid methods are most promising by resolving only the outer boundary layer and massive separation regions.

To date, to the authors' knowledge, there are no numerical or experimental studies of the current case study. Nevertheless, there are works with the same airfoil at different Reynolds numbers and angles of attack, which will serve as a qualitative reference for the results obtained. These works are described below. Chang *et al.* (2022) performs a URANS-type numerical simulation using a standard $\kappa - \omega$ turbulence model and evaluates the vortex shedding structure and the change it produces in lift, drag and surface pressure distribution. Also, it evaluates the downstream vortex structure and flow stability for a range of angles of attack from 0º to 24º at a Reynolds number of 1×10^4.

Pruski and Bowersox (2013), performs an experimental study with Particle Image Velocimetry (PIV) of the flow

structure at the leading edge of a NACA 0012 airfoil under static stall conditions for a Reynolds number of 1.0×10^6 and angle of attack of 16.7º. Measuring and evaluating the time-averaged flow properties (velocity field and Reynolds tensor). Ke and Edwards (2017) contrasts this study by performing hybrid RANS/LES simulations, evaluating the airfoil in free-flow conditions and inside a wind tunnel. He also adds the visualisation of the Q-criterion iso-surfaces where the boundary layer separation is visualised.

In this work, the main objective is to study these phenomena by means of the numerical simulation of the flow inside a wind tunnel on a NACA 0012 airfoil with a chord c = 0.5 m, at high Reynolds number, equal to 1.0×10^6 and at a critical angle of attack of 18º. The OpenFOAM software and the hybrid turbulence model RANS/LES $\kappa\omega_{SST}DDES$ proposed by Gritskevich *et al.* (2012) have been used to carry out the simulations.

In summary, our work consists of simulating a NACA 0012 airfoil under stall conditions and contrasting the results with the previously cited authors. The paper is organised as follows: Section 2 describes the numerical methodology. Section 3 describes the simulation setup and discretisation schemes. Section 4 presents and discusses results. Section 5 conclusions and future work.

2. COMPUTATIONAL MODEL

This section outlines the numerical methodology used in this work. Presenting first the governing equations and then details of the software and solver used in the computational implementation.

2.1 Governing equations

The flow over the airfoil flows at a Mach value less than M<1. Therefore, the equations governing the incompressible flow problem will be written in their conservative form. Hybrid RANS/LES methods divide the domain into two regions and apply different equations that model turbulence in each of them. In regions close to the wall the RANS equations are solved. In the other region, the Navier-Stokes equations filtered by the LES model are solved. In this sense, the semi-discrete governing equations are as follows:

$$\int_{\Omega} \frac{\partial \boldsymbol{u}}{\partial t} d\Omega + \int_{\Gamma} \boldsymbol{u}(\boldsymbol{u} \cdot \boldsymbol{d\Gamma}) = -\int_{\Omega} \boldsymbol{\nabla}P d\Omega + \int_{\Gamma} \nu \left[\boldsymbol{\nabla u} + (\boldsymbol{\nabla u})^T \right] \cdot \boldsymbol{d\Gamma} + \int_{\Gamma} \boldsymbol{\tau'} \cdot \boldsymbol{d\Gamma} \qquad (1)$$

$$\int_{\Gamma} \boldsymbol{u} \cdot \boldsymbol{d\Gamma} = 0 \qquad (2)$$

where "Eq. 1" is the momentum balance, "Eq. 2" the mass balance, Ω the volumetric domain, Γ surface, $\boldsymbol{u}$ the velocity, $P = p/\rho$ pressure normalized by the fluid density, ν kinematic viscosity and $\boldsymbol{\tau'}$ is the stress tensor that represents the modeled turbulent scales.

2.2 Computational implementation

As specified previously, the simulations were carried out with the OpenFOAM finite volume platform. The pressure-velocity coupling algorithm used in this work is PIMPLE, implemented in the pimpleFoam solver. This solver works by combining the PISO and SIMPLE algorithms, being able to control the internal and external loops, together with the under-relaxation coefficients (Holzmann, 2019). This approach allows maintaining temporal precision in transient simulations with second-order temporal schemes, even for Courant numbers greater than one (Greenshields and Weller, 2022).

3. SIMULATION SETUP

In this section the dimensions of the computational domain and meshing strategies are described. In addition, the temporal-spatial discretization schemes used are detailed.

3.1 Computational domain and airfoil location

In an initial stage, the aim was to simulate the airfoil within the complete section of the wind tunnel of the National University of the Northeast (Wittwer and Möller, 2000). The computational cost of simulating an airfoil with a span greater than its chord is too high. Therefore, the wind tunnel section is partially represented by adopting a quasi-3D model of the airfoil and periodic boundary conditions on the wind tunnel side walls. For this reason, we adopt a 0.2 meter width for the computational domain and the span. This strategy allows simulating turbulent flow without violating its three-dimensional characteristic. "Figure 1" presents the dimension of the computational domain, the location of the

airfoil and the boundary conditions: inlet velocity and associated turbulence intensity; at the roof and floor the no slip no slip condition and the relative outlet pressure.
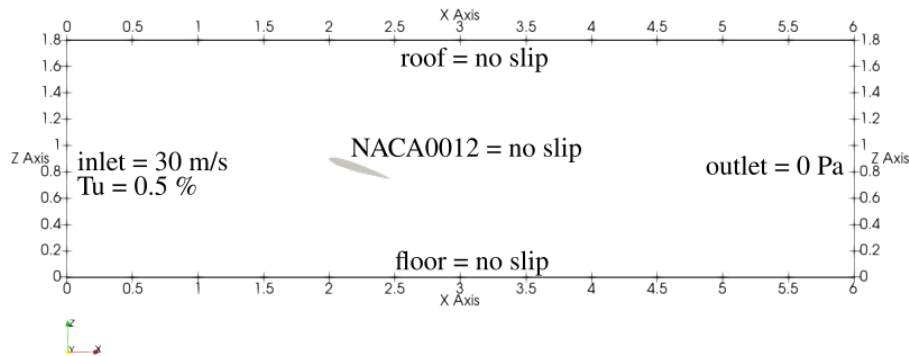

Figure 1. Side view of the computational domain.

3.2 Initial mesh

This mesh is used to carry out the initial studies. The applications used "blockMesh" and "snappyHexMesh", native to OpenFoam, generate cells of hexahedral typology. Three zones are defined with different mesh density levels, a background zone with the size of cells according to the blocks defined in the blockMesh, and the rest by the densification of those background cells with respect to an order of $2^{(levels)}$ detailed in the "Tab. 1". By defining these zones, we seek to activate the LES model to calculate the eddies generated by the deatchment of the boundary layer downstream of the leading edge and in the wake near the airfoil.

The edges of the airfoil have been densified with a level 4 and the boundary layer discretized by 7 cells with a maximum total height of 0.934mm and a minimum cell height of 0.0723 mm.
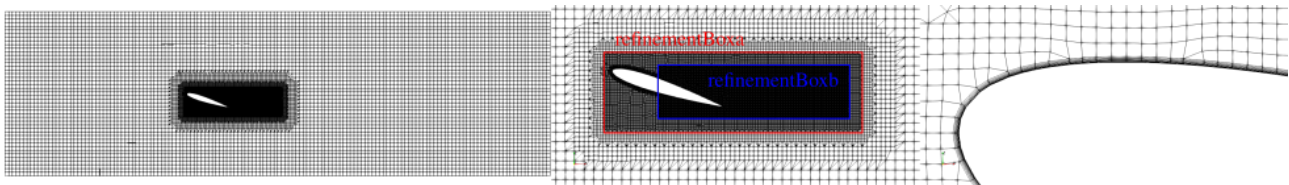

Figure 2. View of meshing strategies in the symmetry plane.

Table 1. Refinement parameters and metrics.

Mesh density (cells)	blockMesh (blocks)	RefinementBoxa (levels)	RefinementBoxb (levels)
3092120	(150 5 45)	(4 4)	(4 3)

3.3 Numerical and discretisation schemes

The temporal and spatial terms of the governing equations are discretised using second-order precision schemes (Travin *et al.*, 2002). The time step was set to 8.12911 $\times 10^{-5}$ s, consistent with a maximum Courant number of 4. The transient problem is solved in a time frame of 4 s, the average solutions calculated from 2 s. The flow passed the airfoil 120 times along its longitudinal extension which guarantees a statistically converged result.

4. RESULTS

In this section, time-averaged flow field results, flow state analysis - vortex shedding frequencies, Q-criterion isosurfaces are presented and discussed. In addition, coherent structures of the turbulent flow and the Power Spectral Density (PSD) of the velocity field will be analyzed at five points in the domain "Fig. 3".

The location of the probes was selected to evaluate the different simulated turbulent flow conditions. The P_0 probe allows evaluating conditions upstream of the airfoil where the flow is undisturbed. The probe P_1 is located in the middle zone of the airfoil near the upper boundary layer. The probe P_2 is located in the vortex street that emerges from the trailing edge. The probes P_3 and P_4 are located even further behind P_2 in order to capture different conditions of the disturbed turbulent flow. It should be noted that the probes P_0 and P_4 are located in the area where the hybrid turbulence model

used resolves turbulent stresses using the RANS method. In the remaining probes the hybrid model uses the LES method.
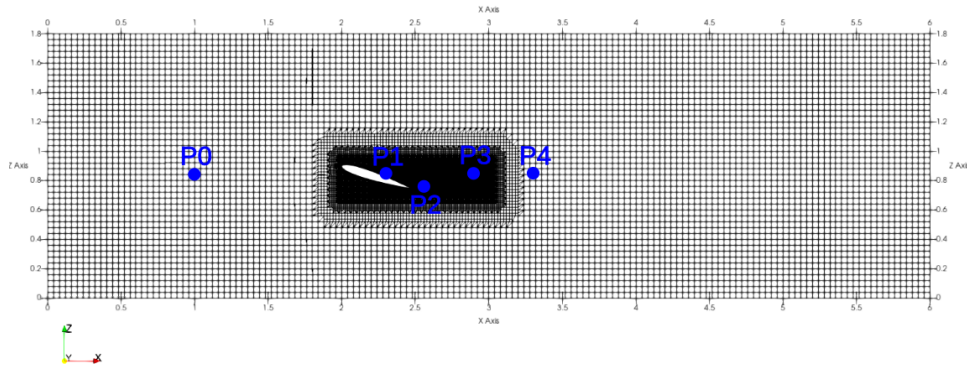

Figure 3. Location of probes in the domain (x y z): P_0 (1 0 0.85), P_1 (2.3 0 0.85), P_2 (2.63 0 0.77), P_3 (2.9 0 0.85), P_4 (3.3 or 0.85).

4.1 Time averaged flow-fied

"Figure 4" shows the flow variables averaged over time. On the left, the normalized average velocity is presented, the flow separation region on the leading edge of the airfoil is observed. At an approximate distance of x/c=0.07. On the right, the Reynolds shear stress tensor shows an increase in values near the indicated separation region. These results compared with the experimental results of Pruski and Bowersox (2013) and the simulations of Ke and Edwards (2017) show similarity in relation to the location of the separation region even though in these works the angle of attack is slightly different.
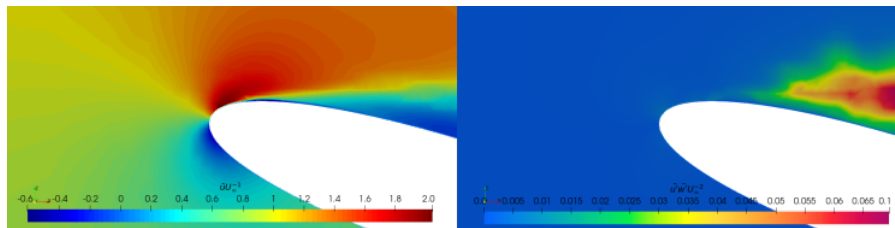

Figure 4. Time-averaged flow properties. On the left: normalized mean velocity $\bar{u}U_\infty^{-1}$. On the right: Reynolds shear stress $\bar{u'w'}U_\infty^{-2}$.

4.2 Flow state analysis - vortex sheeding

"Figure 5", on the left, shows the time series of Cl starting at 2 s. A steady-state behavior of the lift coefficient is observed. On the right, the frequency spectrum is shown, which shows the chaotic state that characterizes the flow state of the evaluated angle. The frequencies of the vortex shedding are similar to those obtained by Chang *et al.* (2022) for chaotic flow states between the angles of attack of 16º to 18º.
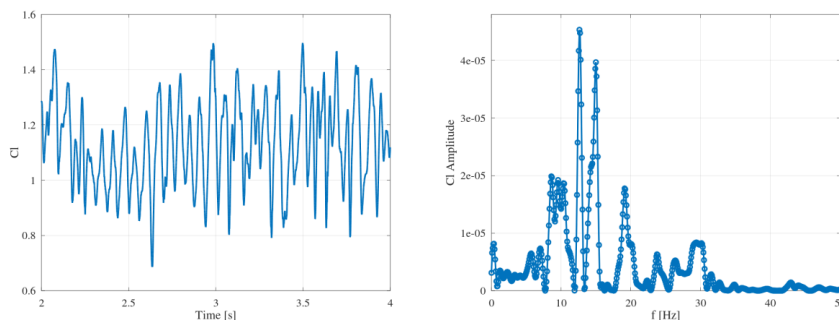

Figure 5. On the left: Cl time series from 2s. On the right: Cl coefficient spectrum.

4.3 Q-criterion iso-surfaces

"Figure 6", shows the Q-criterion isosurfaces for a value $3 \times 10^5 s^{-2}$ where the massive detachment of the boundary layer is evident in the indicated region x/c=0.07. In addition, the formation of vortices downstream of the leading edge is observed. The high Reynolds number makes it impossible to clearly identify stable structures along the airfoil. However, it is possible to observe "hairpin" destabilized vortices in the central zone of the airfoil. Downstream, the predominant development of vortices occurs in the longitudinal direction combined with the other directions. A tendency towards isotropy is observed as they move away from the airfoil.
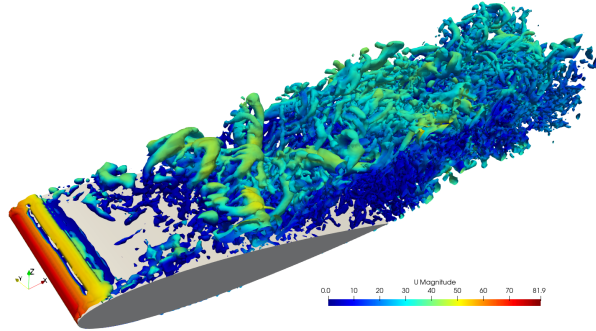

Figure 6. Q-criterion iso-surfaces $3 \times 10^5 s^{-2}$.

4.4 Coherent structures

These structures are patterns or organised regions in the turbulence that allow a more detailed understanding of the flow dynamics. The Reynolds stress tensor represents the average correlations between the fluctuating velocity components. The evaluation of the anisotropy of this tensor allows to understand the directional dependence of these fluctuations (Pope, 2000). In this work, these structures are analyzed by combining the tensor analysis described above and the Q-criterion evaluated in the previous section.

The implementation of this analysis requires the evaluation of the turbulent kinetic energy "Eq. 3", the Reynolds stress tensor "Eq. 4", its anisotropic deviatoric tensor "Eq. 5" and the normalised anisotropic deviatoric tensor "Eq. 6". These equations are presented below. To characterize the anisotropy, two variables η and ξ identified as invariants of the normalized tensor will be used. The use of these variables allows a simple graphical representation (Choi and Lumley, 2001). It should be noted, that the invariants are a function of the eigenvalues λ_i of the normalized anisotropic tensor.

Using the technique described above, the variables η and ξ are calculated for the points defined in the "Fig. 3". The results obtained allow the characterization of the anisotropy state of the turbulent flow at these positions and their graphing in the Lumley triangle "Fig. 7". Any realizable Reynolds stress correspond to a point inside the triangle, while points that are outside correspond to non-realisable Reynolds stresses.

$$\kappa = \frac{1}{2}\bar{u}_i'\bar{u}_i' \tag{3}$$

$$R_{ij} = \bar{u}_i'\bar{u}_j' \tag{4}$$

$$a_{ij} = \bar{u}_i'\bar{u}_j' - \frac{2}{3}\kappa\delta_{ij} \tag{5}$$

$$b_{ij} = \frac{a_{ij}}{2\kappa} \tag{6}$$

$$\eta = \left(-\frac{\lambda_2}{3}\right)^{1/2} \tag{7}$$

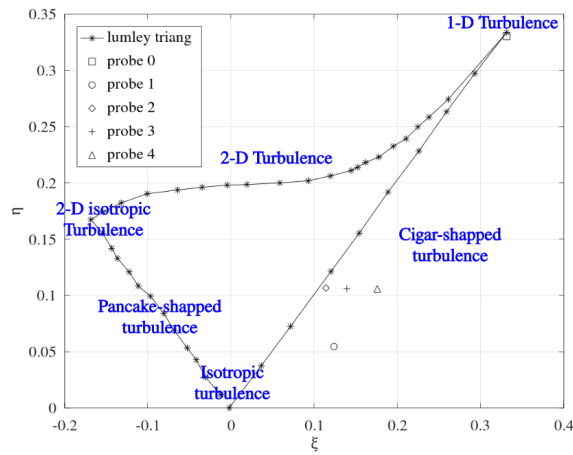$$\xi = \left(\frac{\lambda_3}{2}\right)^{1/3} \tag{8}$$

Figure 7. Lumley triangle

As seen in the "Fig. 7", P_0 is positioned in the 1-D turbulence region, which coincides with the flow in this zone upstream of the airfoil not yet disturbed and with a low level of turbulence intensity . All the remaining points are outside the triangle, therefore it is evident that the hybrid model $\kappa\omega_{SST}DDES$ is not realizable and that it has difficulties in correctly modeling the structures that the disturbed turbulent flow has. In a way, the distance of these external points from the triangle indicates how synthetic the simulation is, how far from reality it is.

The P_1 indicates that the turbulence has a cigar shape with predominance of longitudinal development in combination with a tendency towards isotropy. The P_2 is the closest to the triangle, evidencing a better capacity of the simulation to predict the structures in the vicinity of the trailing edge for cases where the AoA is critical, also here the turbulence has a predominantly longitudinal or cigar shape. The P_3 and P_4 have similar characteristics to the previous point analyzed. However, P_4 is the one with the worst performance of the external points, because at this point the hybrid model uses the RANS method unlike the rest that use the LES method. All these evaluated points have a cigar-shaped turbulent structure of longitudinal development in combination with dissipation effects (isotropy) that alter the formation of easily identifiable stable structures and that were previously also presented through the evaluation of the Q-criterion iso surfaces "Fig. 6".

4.5 Power Spectral Density (PSD)

The fluctuating signals of the velocity field u_i', for the five points defined in the "Fig. 3" are analysed after 2 seconds. The calculation of the spectra of these signals is performed with the Welch's method (Welch, 1967); Hann's window function is used; defined in blocks of 2^{12} elements; with an overlap of 50%; the total length of the signal is evaluated with a sampling frequency equivalent to the time step specified in the time discretisation.

"Figure 8"; "Fig. 9"; "Fig. 10"; "Fig. 11" and "Fig. 12" below, shows the fluctuating velocity signals u_n', v_n', w_n' with their RMS values, and their spectra Su_n, Sv_n, Sw_n, where n represents the analysed point.

"Figure 8", shows on the left, the fluctuating components of the velocity vector at P_0. The turbulence intensity levels are all less than 0.5%, in agreement with those imposed by the boundary condition. On the right, the (PSD) curves shows the low energy content and the inability of the RANS model used in this region by the hybrid turbulence model to resolve the frequencies of the inertial subrange. This is evidenced by the non-parallelism of the spectrum in this range with the Kolmogorov -5/3 slope. In addition, an energy disparity is evident, where S_{v0} has even lower energy than S_{u0} S_{w0}, may be due to the fact that the turbulent flow has not yet been perturbed and is influenced by the hypothesis of the quasi-3D analysis model.

"Figure 9", shows on the left, the fluctuating components of the velocity vector at P_1. The turbulence intensity levels are much higher than those at P_0. The turbulence intensity in all directions is in the range of 18% to 25%. The u_1 component has the highest intensity, followed by w_1 and v_1. On the right, it is observed that the (PSD) curves S_{u1}, S_{v1} and S_{w1}, decay following the slope -5/3 in the inertial subrange. Indicating that the LES model used in this region by the hybrid turbulence model is consistent with the turbulent cascades in that frequency range. In the range below 20 Hz the PSD curves differ slightly, where S_{u1} and S_{w1} have higher energy than S_{v1}. From 20 Hz onwards the curves converge to a similar energy content.

"Figure 10", on the left, shows the fluctuating components of the velocity vector at P_2. The turbulence intensity levels from 21% to 38% are even higher than those at P_1. The component w_2 has the highest intensity, which shows strong vertical velocity fluctuations. The remaining components u_2 and v_2 have somewhat lower turbulence intensities. On the right, it can be seen that the (PSD) curves decay in a similar way as in P_1. In the frequency range 0 to 100 Hz, a higher
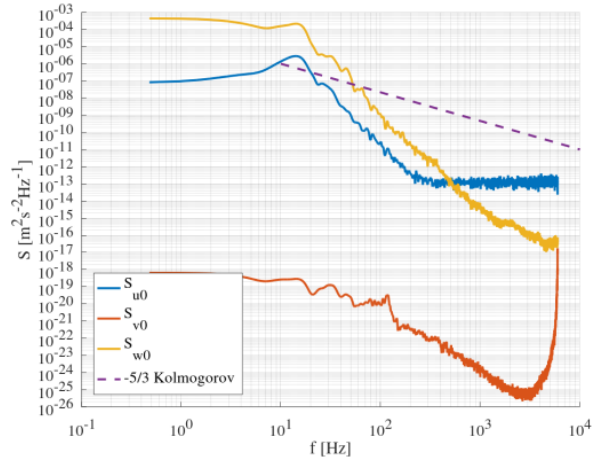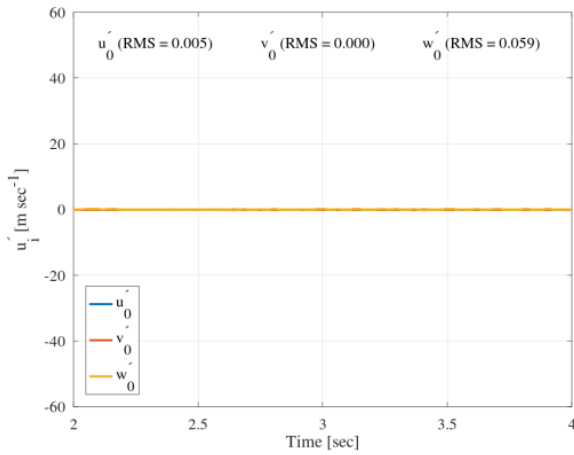
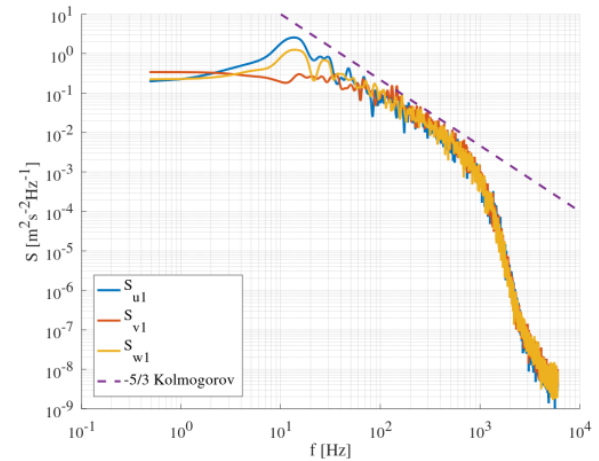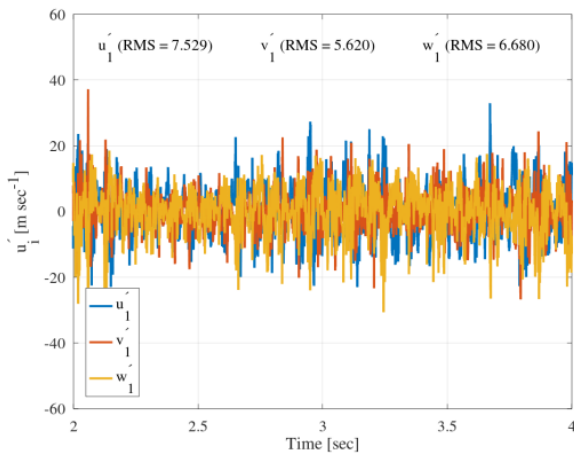Figure 8. Probe 0: Time series data and Power Spectral Density (PSD)

Figure 9. Probe 1: Time series data and Power Spectral Density (PSD)

energy content is evident than in P_1. In the range from 10 to 100 Hz, the component S_{w2} has more energy than S_{u2} and S_{v2}. From 100 Hz onwards, the curves converge to a similar energy content.
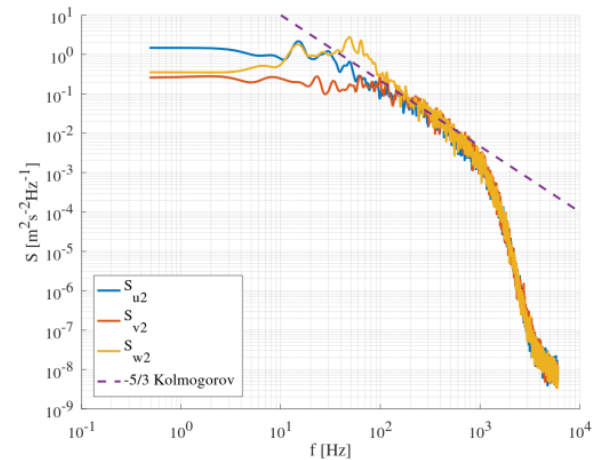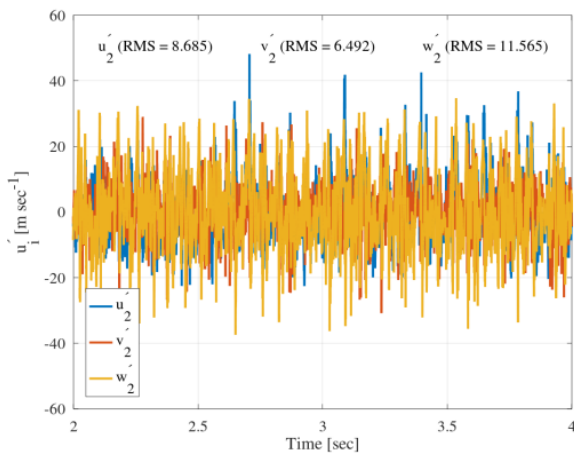

Figure 10. Probe 2: Time series data and Power Spectral Density (PSD)

"Figure 11", shows on the left, the fluctuating components of the velocity vector in P_3. The turbulence intensity levels of 13% to 26%, are somewhat lower than those of P_2. The component w_3 has the highest turbulence intensity, followed in decreasing order by u_3 and v_3. On the right, it is observed that the curves (PSD) decay in a similar way as in P_1 and

P_2. In the range from 0 to 100 Hz the energy content is much lower than P_2. Between 0 and 25 Hz S_{u3} has more energy than S_{w3} and S_{v3}. Between 25 and 100 Hz S_{w3} has more energy than S_{u3} and S_{v3}. From 100 Hz onwards the curves converge to a similar energy content.
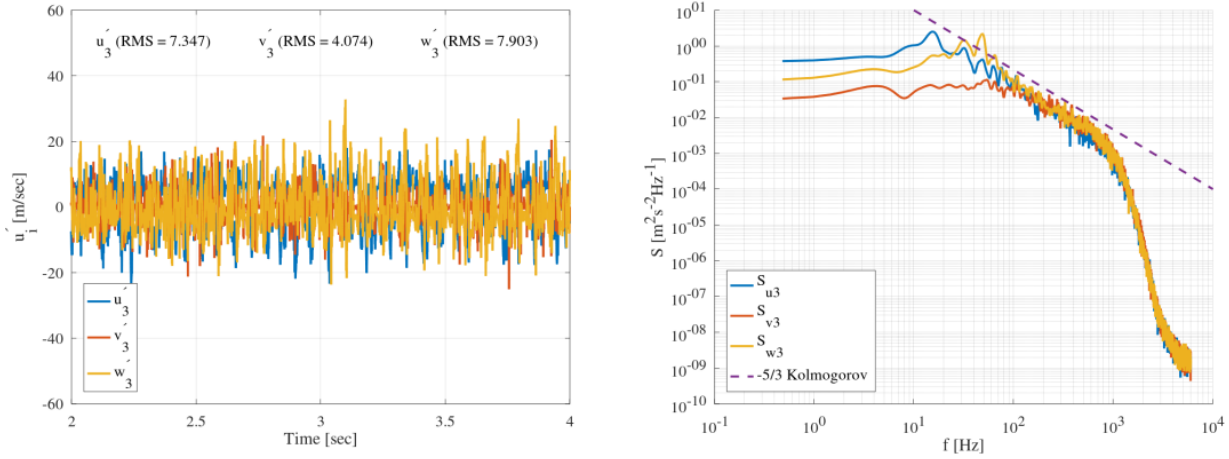

Figure 11. Probe 3: Time series data and Power Spectral Density (PSD)

"Figure 12", shows on the left, the fluctuating components of the velocity vector at P_4. The turbulence intensity levels from 4% to 20% are lower than those of P_1, P_2 and P_3. But higher than P_0. The component w_4 has the highest turbulence intensity, followed in decreasing order by u_4 and v_4. On the right, it is observed that the curves (PSD) do not decay in a similar way to those of the points P_1, P_2 and P_3. Indicating that the RANS model used in this region by the hybrid turbulence model fails to resolve the inertial subrange. In the range from 0 to 100 Hz the energy content is lower than P_3. Between 0 and 25 Hz S_{u3} has more energy than S_{w3} and S_{v3}. Between 25 and 100 Hz S_{w3} has more energy than S_{u3} and S_{v3}. From 100 Hz onwards the energy content of the curves is similar, but the decay is premature and they do not follow the -5/3 Kolmogorov slope.
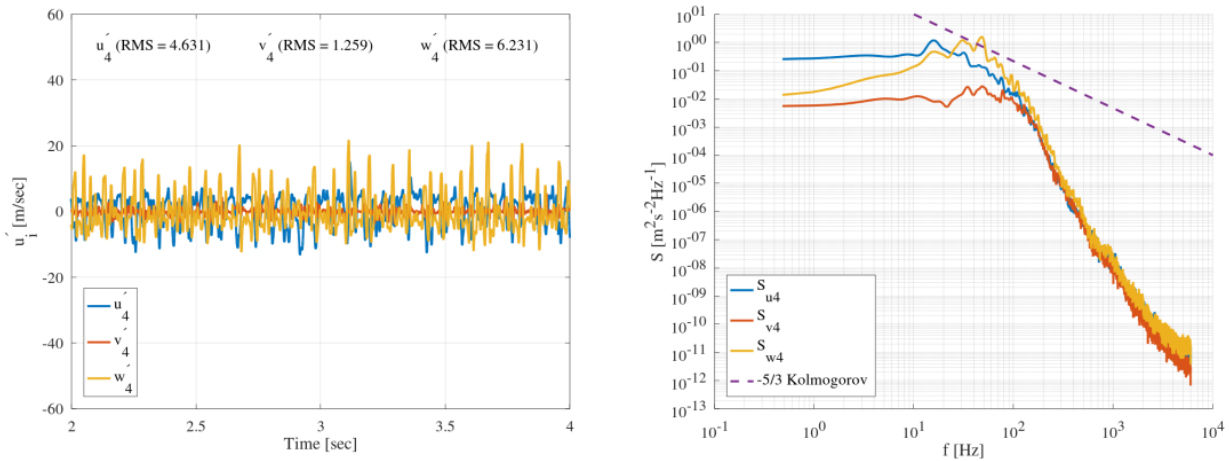

Figure 12. Probe 4: Time series data and Power Spectral Density (PSD)

5. CONCLUSIONS

In this work, the mean flow velocities, the stability of the vortices over the airfoil, the coherent shapes of the turbulent structures by means of the analysis of the iso-surfaces generated with the Q-Criterion have been studied. In addition, the degree of anisotropy and the predominant shape of the coherent structures in them have been evaluated at five points of the domain. An analysis of turbulence intensities and energy contents of the PSD curves has also been carried out for each of the points. Although the works used for the comparison do not have the same configurations, they serve to evaluate the solution of the turbulent flow in conditions of similar flow.

These results were obtained by using the hybrid turbulence model $\kappa\omega_{SST}DDES$ in the simulation. This model has strengths and limitations. Therefore, it is possible to conclude that the model manages to characterize without too much

difficulty the dynamic forces that act on the body, obtaining good results also in the analysis of the averaged flow and the aerodynamic configuration on the airfoil. Furthermore, it manages to capture the characteristic massive detachment of the boundary layer over the upper surface in the critical AoA configuration (18º). In the wake, the turbulent flow is resolved with certain limitations. The analysis of the coherent structures for the five points of the domain shows a limitation of the model in obtaining results that are not feasible for the normalized deviatoric tensor. In the analysis of the PSD curves, a possible overestimation of the turbulent kinetic energy at the points located in the wake is observed, due to the effects of insufficient dissipation of the momentum of the smallest turbulent scales and an amplification of the wake caused by the overestimation of the shear stresses in the boundary layer.

It should be noted that the mesh used has difficulties in capturing the behavior of the detached flow. It is possible to improve it in future works by increasing its density in the areas of massive detachment. Also, in future works it would be possible to add simulation time to capture the lowest frequencies of the turbulent flow in better detail.

6. REFERENCES

Chang, J., Zhang, Q., He, L. and Zhou, Y., 2022. "Shedding vortex characteristics analysis of naca 0012 airfoil at low reynolds numbers". *Energy Reports*, Vol. 8, pp. 156–174. ISSN 2352-4847. doi:10.1016/j.egyr.2022.01.149. 2021 International Conference on New Energy and Power Engineering.

Choi, K.S. and Lumley, J.L., 2001. "The return to isotropy of homogeneous turbulence". *Journal of Fluid Mechanics*, Vol. 436, p. 59–84. doi:10.1017/S002211200100386X.

Greenshields, C. and Weller, H., 2022. *Notes on Computational Fluid Dynamics: General Principles*. CFD Direct Ltd.

Gritskevich, M.S., Garbaruk, A.V., Schütze, J. and Menter, F.R., 2012. "Development of DDES and IDDES formulations for the $\kappa\omega$ shear stress transport model". *Flow, Turbulence and Combustion*, Vol. 88, No. 3, pp. 431–449. doi: https://doi.org/10.1007/s10494-011-9378-4.

Holzmann, T., 2019. *Mathematics, Numerics, Derivations and OpenFOAM*. Holzmann CFD, 7th edition.

Ke, J. and Edwards, J.R., 2017. "Numerical simulations of turbulent flow over airfoils near and during static stall". *Journal of Aircraft*, Vol. 54, No. 5, pp. 1960–1978. doi:10.2514/1.C034186.

Pope, S.B., 2000. *Turbulent Flows*. Cambridge University Press.

Pruski, B.J. and Bowersox, R.D.W., 2013. "Leading-edge flow structure of a dynamically pitching naca 0012 airfoil". *AIAA Journal*, Vol. 51, No. 5, pp. 1042–1053. doi:10.2514/1.J051673.

Travin, A.and Shur, M., Strelets, M. and Spalart, P.R., 2002. "Physical and numerical upgrades in the detached-eddy simulation of complex turbulent flows". In R. Friedrich and W. Rodi, eds., *Advances in LES of Complex Flows*. Springer Netherlands, Dordrecht, pp. 239–254. ISBN 978-0-306-48383-7.

Welch, P., 1967. "The use of fast fourier transform for the estimation of power spectra: A method based on time averaging over short, modified periodograms". *IEEE Transactions on Audio and Electroacoustics*, Vol. 15, No. 2, pp. 70–73. doi:10.1109/TAU.1967.1161901.

Wittwer, A. and Möller, S., 2000. "Characteristics of the low-speed wind tunnel of the unne". *Journal of Wind Engineering and Industrial Aerodynamics*, Vol. 84, pp. 307–320. doi:10.1016/S0167-6105(99)00110-5.